

## In-Flight Measurements of Capsule Shell Adiabats in Laser-Driven Implosions

A. L. Kritcher,<sup>1</sup> T. Döppner,<sup>1</sup> C. Fortmann,<sup>1,2</sup> T. Ma,<sup>1</sup> O. L. Landen,<sup>1</sup> R. Wallace,<sup>1</sup> and S. H. Glenzer<sup>1</sup>

<sup>1</sup>*L-493, Lawrence Livermore National Laboratory, P.O. Box 808, Livermore, California 94551, USA*

<sup>2</sup>*Department of Physics and Astronomy, University of California, Los Angeles, California 90095, USA*

(Received 11 March 2011; published 1 July 2011)

We present the first x-ray Thomson scattering measurements of temperature and density from spherically imploding matter. The shape of the Compton downscattered spectrum provides a first-principles measurement of the electron velocity distribution function, dependent on  $T_e$  and the Fermi temperature  $T_F \sim n_e^{2/3}$ . In-flight compressions of Be and CH targets reach 6–13 times solid density, with  $T_e/T_F \sim 0.4$ – $0.7$  and  $\Gamma_{ii} \sim 5$ , resulting in minimum adiabats of  $\sim 1.6$ – $2$ . These measurements are consistent with low-entropy implosions and predictions by radiation-hydrodynamic modeling.

DOI: 10.1103/PhysRevLett.107.015002

PACS numbers: 52.57.-z, 52.50.Jm, 52.59.Hq, 52.70.-m

The study of the microscopic properties of dense matter has gained considerable interest in the last few years, as experiments are under way [1–7] to achieve inertial confinement fusion (ICF) [8,9] at the National Ignition Facility (NIF) [10]. These experiments are designed to achieve highly compressed states of matter, approaching  $1000 \text{ g/cm}^3$  in a cold dense  $D$ - $T$  shell surrounding a central hot-spot plasma. The capsule is tuned by shaping the laser power, thereby launching a series of four coalescing shock waves to achieve the desired high fuel densities. The timing and strength of these shocks are important for compressing the solid density target on a low adiabat, i.e., to achieve a low-entropy implosion [11]. Furthermore, equation of state measurements at subnuclear densities are important for calculations that model stellar collapse. Here, the entropy per nucleon is conserved to a good approximation and studying the plasma properties of strongly coupled matter along a constant adiabat is of particular interest [12,13]. Thus, it is important to directly characterize cold and highly compressed plasma states with the goal to validate integrated modeling of spherically imploding matter.

In this Letter we present the first simultaneous measurement of the electron density and electron temperature of spherically convergent matter via spectrally resolved x-ray Thomson scattering. We determine in-flight adiabats of 1.6–2, approaching the desired adiabat of 1.5 for implosions driven by shaped laser pulses [14]. While Thomson scattering has previously been applied to planar shock systems [15–21], here we employ high-energy x rays at  $\sim 9 \text{ keV}$  to characterize matter densities of  $n_e > 10^{24} \text{ cm}^{-3}$  at the 30 kJ Omega laser facility [22]. Our signal to noise ratios (SNR) of  $\sim 200$  obtained at these densities indicate the ability for single-shot characterization of imploding targets resulting in a  $\pm 20\%$  error bar on electron density and temperature if both parameters are simultaneously determined. Measurement of the temperature and density enables inferring of the time-resolved CH and Be capsule adiabats, that can be used to test

low-adiabat laser pulse shaping [11] and models that predict shock timing for spherically convergent targets.

Probing of the microscopic plasma properties results in both elastic and inelastic scattering features. The intensity of the elastic scattering is sensitive to the static structure factor of the material. The Compton feature provides a direct measure of the electron velocity distribution. For these weakly degenerate plasmas, the velocity distribution is in between a Thomas-Fermi ( $T_e = 0$ ) and a Boltzmann distribution ( $T_e \gg T_F$ ). The width of the inelastic Compton feature is sensitive to the Fermi temperature  $T_F$ , which is only dependent on electron density, and the shape of the red wing is sensitive to electron temperature  $T_e$  [23]. Thus, the temperature and density are simultaneously determined from first principles by accurately measuring the Compton feature width and shape.

Figure 1 shows a schematic of the experimental configuration. In these experiments, CH and Be capsules (outer diameter =  $860 \mu\text{m}$ ,  $\rho_{o,\text{Be}} = 1.85 \text{ g cm}^{-3}$ ,  $\rho_{o,\text{CH}} = 1.1 \text{ g cm}^{-3}$ , 40–45  $\mu\text{m}$  thick) have been compressed and heated in a spherical geometry by  $\sim 15 \text{ kJ}$  of 351-nm laser light. The laser light was delivered by 36 shaped drive beams (with  $\sim 0.6 \text{ TW}$  in a 1 ns foot and  $\sim 15 \text{ TW}$  in a 1 ns peak, see Fig. 1) [24–26]. Self-emission from the capsules enables probing of the shell radius for  $t < 2.9 \text{ ns}$ . Also shown in Fig. 1 are measured radii overlaid on radiation-hydrodynamic simulations of the shell mass density as function of time and shell radius. Here,  $t = 0 \text{ ns}$  denotes the start of the drive beams. At  $t = 2 \text{ ns}$  when the laser pulse has turned off, self-emission images of the imploding shells become extremely noisy, leading to the larger error bars. At  $t > 2.9 \text{ ns}$ , no images could be recorded. In order to enable probing of extremely high-energy density conditions later in the implosion and to measure the adiabat, we employ x-ray Thomson scattering [15].

To characterize the compressed shells with x-ray scattering, a laser-produced zinc He- $\alpha$  x-ray source delayed in time from the compression beams was scattered from the targets at  $135 \pm 15^\circ$ , accessing the noncollective regime.

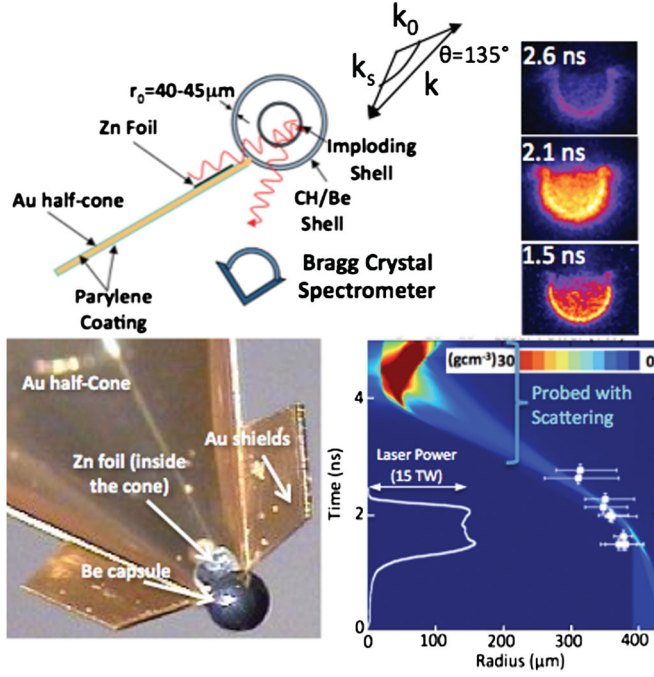


FIG. 1 (color). (top) Illustration of the target and self-emission images of imploding Be shells. (bottom) Photo of a Be cone-in-half-shell target and radiation-hydrodynamic modeling of the imploding shell mass density vs radius and time. The white data points are measured radii from self-emission images and the white curve is the laser power profile vs time.

The Zn He- $\alpha$  x-ray source (9 keV) was produced using 7–9 additional shaped laser beams ( $5.5 \times 10^{15}$  W cm $^{-2}$ , see Fig. 1) that irradiated 10  $\mu$ m thick Zn foils, mounted onto gold half-cones attached to the capsules. The gold cones (length 7 mm, 60  $\mu$ m thick, 60° opening) ensured that the crystal spectrometer detected only scattered x rays from the implosion. Additional gold shields were used to block potential Zn emission from plasma expansion around the cone. The gold cones and shields were coated with 10  $\mu$ m thick Parylene to reduce bremsstrahlung emission from hot electrons. The scattered x rays were measured using a high efficiency, high-energy resolution highly oriented pyrolytic graphite (HOPG) crystal spectrometer coupled to an x-ray framing camera with a gate time of 180 ps and a CCD detector. Additional diagnostics include a streaked crystal spectrometer used to measure the Zn probe emission as a function of time for each shot, and pinhole cameras that yield temporally resolved images of the ablator emission during the drive laser pulse.

In these experiments noncollective behavior of the plasma was measured, where the scattering parameter  $\alpha_e = 1/k\lambda_S = hc/(E_0 2\pi\lambda_S) < 1$ . Here,  $k$  is the magnitude of the scattering vector, where  $k = (4\pi E_0/hc) \times \sin(\theta_S/2)$ , and  $\lambda_S$  is the Debye or Thomas-Fermi screening length. The scattering regime can be set by choosing the energy of the incident probe x rays,  $E_0$ , and the angle of the detected scattered x rays,  $\theta_S$ . For the conditions in this

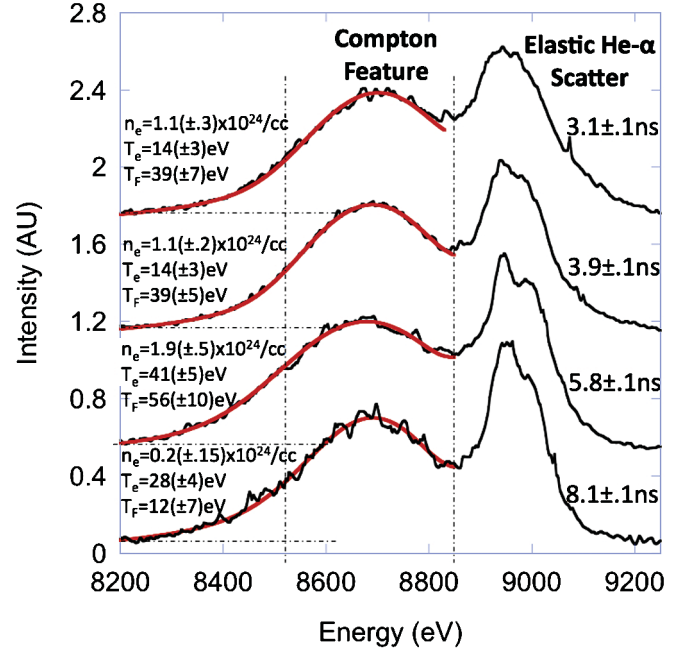


FIG. 2 (color). Measured (black) and best fits (red) to the Compton feature of the scattered x-ray spectra from Be implosions at various times, yielding  $n_e$  and  $T_e$ .

experiment,  $E_0 = 9$  keV and  $\theta_S = 135 \pm 15^\circ$ , the scattering parameter  $\alpha_e \sim 0.27$ .

Figure 2 shows measured x-ray scattering spectra from spherically driven Be capsules at  $t = 3.1 \pm 0.1$  ns and  $3.9 \pm 0.1$  ns, before maximum convergence, at  $t = 5.7 \pm 0.1$  ns, about the time of maximum convergence, and  $t = 8.1 \pm 0.1$  ns, after maximum convergence. We observe elastic scattering at  $\sim 9$  keV and inelastic Compton scattering at  $\sim 8.7$  keV. The Compton feature is downshifted by the Compton energy,  $\Delta E_C \sim 260$  eV, and spectrally broadened by the electron velocity distribution due to Doppler shifting in the field of view of the detector. For our conditions of a weakly degenerate plasma, the width of the Compton feature is mainly sensitive to changes in the Fermi energy ( $T_F^{1/2} \sim n_e^{1/3}$ ). The shape of the red wing is used to extract additional information on  $T_e$ . In these experiments the high SNR of our data enables highly resolved measurements of the Compton red wing shape, thus allowing us to obtain a model-independent measure of  $T_e$  from the electron velocity distribution.

At  $t = 3.1 \pm 0.1$  and  $t = 3.9 \pm 0.1$  ns the best theoretical fits of the electron velocity distribution to the experimental Compton spectra yield  $T_e = (14 \pm 3)$  eV,  $n_e = (1.1 \pm 0.2) \times 10^{24}$  cm $^{-3}$ , and Be(+2). For scattering at  $t = 5.8 \pm 0.1$  ns, fits yield  $T_e = (41 \pm 5)$  eV,  $n_e = (1.9 \pm 0.5) \times 10^{24}$  cm $^{-3}$ , and Be(+2.5), resulting in  $6(\pm 1.5) \times$  solid density at near peak compression. At  $t = 8.1 \pm 0.1$  ns the temperature and density decrease to  $(24 \pm 2)$  eV,  $n_e = (0.2 \pm 0.15) \times 10^{24}$  cm $^{-3}$ , and Be(+2) indicating that the shell is hydrodynamically expanding

and cooling. These measurements are density weighted and spatially averaged over the compressed region of the shell. The ionization state has been measured within 25% from the scattering of weakly bound electrons resulting in a continuum with a tail shifted beyond the red wing of the Compton feature [15]. These measurements are consistent with previous Be ionization data at similar temperatures [15]. For CH, the ionization state is determined within an error of 20%, in agreement with previous CH ionization data at similar temperatures [27].

In Fig. 3 (top), root mean squared (rms) values of theoretical fits to the experimental data at  $t = 3.9 \pm 0.1$  ns shows sensitivity in determining both the electron density and temperature ( $T_e = T_i$ ) simultaneously from the shape of the electron velocity distribution. The dark island in the center of the plot is the range of best fits to the experimental data. Figure 3 (bottom) shows experimental data at  $t = 3.9 \pm 0.1$  ns plotted with calculations of the Thomson scattered spectra for varying  $T_e$  and  $n_e$ . Figure 3(a) shows sensitivity of the Compton feature red wing to changes in  $T_e$  for a fixed electron density and ionization state of  $1.1 \times 10^{24} \text{ cm}^{-3}$  and Be(+2). Shown in Fig. 3(b) is the sensitivity of the Compton feature width to electron density for a fixed electron temperature of 14 eV and ionization state of Be(+2). Figure 3 (bottom) shows fitting to the data that becomes too steep (c) and too parabolic (d) to fit the slope of the Compton feature red wing, as  $T_e$  and  $n_e$  are simultaneously varied. Figure 3 (top) shows that if either  $n_e$  or  $T_e$  is known, the other parameter can be determined within  $\pm 11\%$ . However, determining both  $n_e$  and  $T_e$  from the Compton spectra, yields error bars of  $\pm 20\%$ .

Temporally resolved measurements of the electron temperature, electron density, and ionization state enable determining of the adiabat, defined as the ratio of total electron and ion pressure to electron Fermi pressure, given to within a few percent for  $T_e < T_F$  and to better than 10% for  $T_e > T_F$  as

$$\alpha = \frac{n_e T_F (3/5) \sqrt{[1 + 8.2(T_e/T_F)^2]} + n_i T_i}{n_e (3/5) T_F}. \quad (1)$$

Here,  $T_e$ ,  $T_i$ , and  $T_F$  are the electron temperature, ion temperature, and  $T_F \sim n_e^{2/3}$ , respectively. We assume that the electron and ion temperatures are equal in these strongly collisional plasmas.

Figure 4 (top) shows the adiabat for spherically compressed CH and Be shells. Also plotted are 1D radiation-hydrodynamic simulations of the adiabat as a function of time using HELIOS [28]. The simulations are density weighted and radial variations over the compressed region in 1D are taken into account. The simulation bands reflect the minimum predicted adiabat (lower bound) and an upper bound for the density and temperature weighted adiabat over the compressed shell region that contributes to the scattering spectra (upper bound). The error bars of the

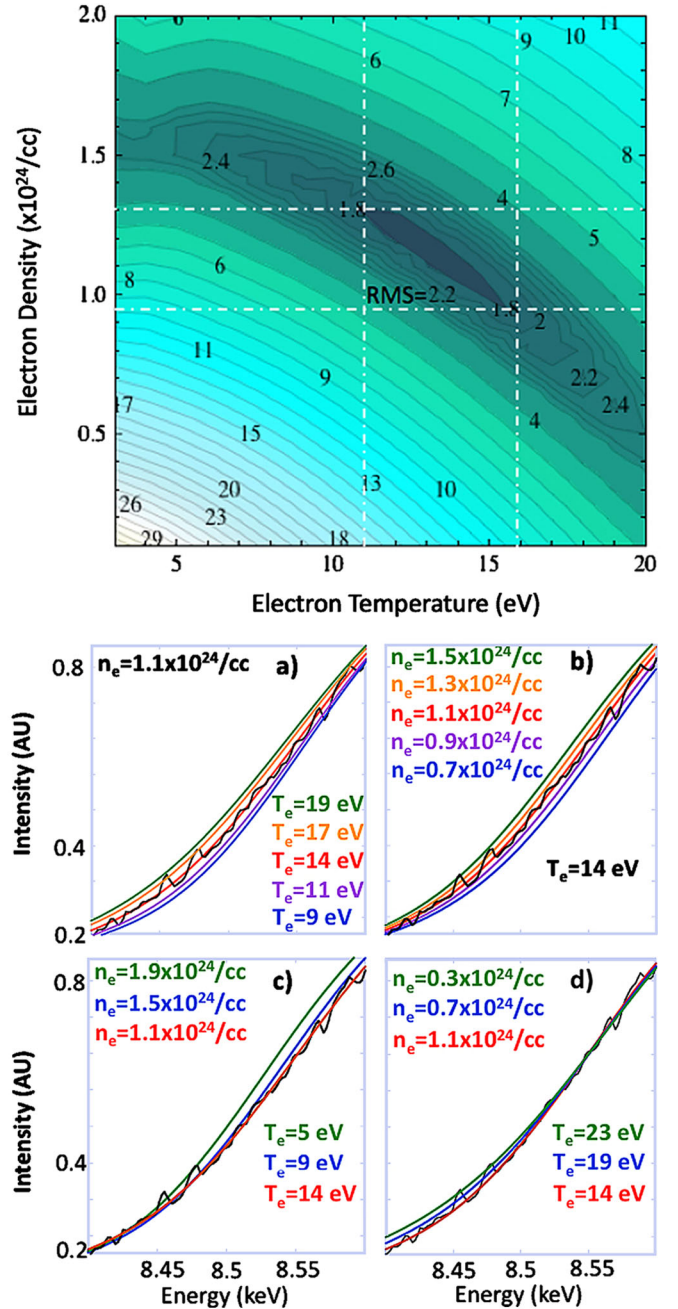


FIG. 3 (color online). (top) Example of rms fits of the experimental Compton feature for Be scattering data taken at  $3.9 \pm 0.1$  ns. (bottom) Fits plotted together with the measured Compton red wings for varying electron temperature and density.

measured adiabats reflect the error in determining  $T_e$ ,  $n_e$ , and ionization state. Plotted in Fig. 4 (bottom) is the ion coupling parameter  $\Gamma_{ii} = (Ze)^2 / (4\pi\epsilon_0 a k_B T_i)$ , where  $a = (4/3\pi n_i)^{-1/3}$  showing that the strongly coupled plasma regime is probed,  $\Gamma > 1$ .

While the in-flight adiabats for Be and CH are similar, the CH capsules reach compressions of up to  $12 \times$  solid density, whereas the maximum observed Be capsule

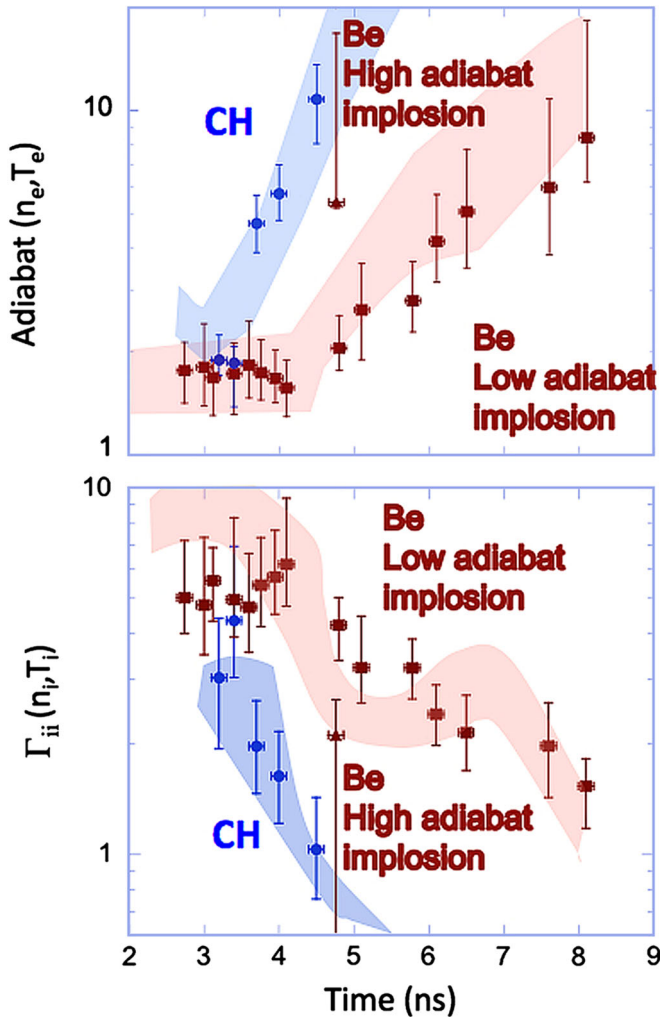


FIG. 4 (color online). Adiabat (top) and ion-ion coupling parameter (bottom) plotted as function of time for compressed Be and CH ablators. Also plotted are 1D radiation-hydrodynamic calculations.

compression is  $6 \times$  solid density. Higher CH densities are reached by compressing a lower initial mass ( $0.9 \times 10^{-4}$  g) than for the Be capsules ( $1.8 \times 10^{-4}$  g) with the same laser drive conditions. The steep adiabat increase after maximum convergence happens earlier for CH than for Be, as expected for compressing lower density capsules with the same drive parameters. The simulated timing of the adiabat increase roughly agrees with experimental measurements for Be and CH. Measurements indicate a near optimum adiabat of  $\alpha = 1.5$ , necessary for ignition, can be reached for both CH and Be with the pulse shaping described in this work. In contrast, when the laser drive conditions are untuned, e.g., using a similar pulse shape with only  $\sim 40\%$  of the drive energy and a peak-to-foot intensity ratio of  $\sim 125$  compared to  $\sim 27$  used in this work, the Be capsule adiabat at near peak compression increases to  $\geq 5$ , also shown in Fig. 4.

In summary, we have accurately measured the model-independent temperature and density of highly compressed targets,  $n_e > 10^{24}$  cm $^{-3}$ . We have also measured the adiabat of spherically compressed CH and Be capsules. These measurements show that the adiabat can be tuned for both CH and Be to the near optimum levels needed for ignition through laser pulse shape tuning. High-quality data obtained in these experiments indicates the ability for single-shot characterization of ICF targets. The SNR ratio of the data  $\sim 200$  provides a basis for future adiabat and dense matter studies of high density matter using this platform. In addition, information on the elastic scattering component for well defined density and temperature conditions will enable future tests of dense matter structure factor models.

This work was performed under the auspices of the U.S. Department of Energy by Lawrence Livermore National Laboratory under Contract No. DE-AC52-07NA27344 and supported by Laboratory Directed Research and Development Grant No. 11-ER-050. C.F. is supported by the Humboldt Foundation. Thanks to R. Bahukutumbi for discussions on pulse shaping.

- 
- [1] J. L. Kline *et al.*, *Phys. Rev. Lett.* **106**, 085003 (2011).
  - [2] S. H. Glenzer *et al.*, *Phys. Rev. Lett.* **106**, 085004 (2011).
  - [3] S. H. Glenzer *et al.*, *Science* **327**, 1228 (2010).
  - [4] E. L. Dewald *et al.*, *Rev. Sci. Instrum.* **81**, 10D938 (2010).
  - [5] P. Michel *et al.*, *Phys. Rev. Lett.* **102**, 025004 (2009).
  - [6] N. B. Meezan *et al.*, *Phys. Plasmas* **17**, 056304 (2010).
  - [7] G. A. Kyrala *et al.*, *Rev. Sci. Instrum.* **81**, 10E316 (2010).
  - [8] J. Nuckolls *et al.*, *Nature (London)* **239**, 139 (1972).
  - [9] J. D. Lindl *et al.*, *Phys. Plasmas* **11**, 339 (2004).
  - [10] E. I. Moses *et al.*, *Phys. Plasmas* **16**, 041006 (2009).
  - [11] S. W. Haan *et al.*, *Nucl. Fusion* **44**, S171 (2004).
  - [12] S. Marcos *et al.*, *Nucl. Phys.* **A381**, 507 (1982).
  - [13] C. J. Pethick *et al.*, *Nucl. Phys.* **A414**, 517 (1984).
  - [14] R. Betti *et al.*, *Phys. Rev. Lett.* **98**, 155001 (2007).
  - [15] S. H. Glenzer *et al.*, *Rev. Mod. Phys.* **81**, 1625 (2009).
  - [16] G. Gregori *et al.*, *Phys. Rev. Lett.* **101**, 045003 (2008).
  - [17] H. J. Lee *et al.*, *Phys. Rev. Lett.* **102**, 115001 (2009).
  - [18] E. Garcia Saiz *et al.*, *Nature Phys.* **4**, 940 (2008).
  - [19] A. L. Kritcher *et al.*, *Science* **322**, 69 (2008).
  - [20] B. Barbrel *et al.*, *Phys. Rev. Lett.* **102**, 165004 (2009).
  - [21] D. Riley *et al.*, *Phys. Rev. Lett.* **84**, 1704 (2000).
  - [22] J. M. Soures *et al.*, *Fusion Technol.* **30**, 492 (1996).
  - [23] O. L. Landen *et al.*, *J. Quant. Spectrosc. Radiat. Transfer* **71**, 465 (2001).
  - [24] C. Zhou *et al.*, *Phys. Rev. Lett.* **98**, 025004 (2007).
  - [25] W. Theobald *et al.*, *Plasma Phys. Controlled Fusion* **51**, 124052 (2009).
  - [26] C. Stoeckl *et al.*, *Plasma Phys. Controlled Fusion* **50**, 124044 (2008).
  - [27] G. Gregori *et al.*, *J. Quant. Spectrosc. Radiat. Transfer* **99**, 225 (2006).
  - [28] J. J. MacFarlane *et al.*, *J. Quant. Spectrosc. Radiat. Transfer* **99**, 381 (2006).